

## Article

# Experimental and Numerical Study on the Low Velocity Impact Behavior of ABR Pipe

Changxi Shan <sup>1</sup>, Shaowei Hu <sup>2,\*</sup> , Xiang Xue <sup>1</sup>, Fuqu Pan <sup>3</sup>, Wenhao Li <sup>1</sup> and Hao Qi <sup>1</sup><sup>1</sup> School of Civil Engineering, Chongqing University, Chongqing 400045, China<sup>2</sup> Yellow River Laboratory, Zhengzhou University, Zhengzhou 450001, China<sup>3</sup> Shandong Dongxin Plastic Technology Co., Ltd., Liaocheng 252000, China

\* Correspondence: hushaowei@zzu.edu.cn

**Abstract:** The low velocity impact load on pipes during transportation, construction and operation will cause pipeline damage and lay hidden dangers for the safety of pipeline engineering. To study the low velocity impact performance of pipes made of acrylate polymer blended with polyvinyl chloride resin for water supply (ABR), 20 sets of specimens with different heights and different masses of drop hammer were carried out to study the mechanical properties of ABR pipes. Based on the impact time curve, the energy dissipation capacity and impact peak value of ABR pipe specimens were analyzed, and the empirical calculation formula of impact force peak based on the test data is obtained by the dimensional analysis method, with a relative error ranging from  $-7.8\%$  to  $4.1\%$ . Moreover, the finite element numerical simulation of ABR pipe specimens subjected to impact load is carried out, and the strain development law and failure mode of the pipe under low-speed impact load are analyzed. Therefore, the calculation formula of peak impact force and failure mode proposed in this paper can provide safety assessment methods for pipeline engineering designers and constructors.

**Keywords:** ABR pipes; low velocity impact; pipe failure; finite elements



**Citation:** Shan, C.; Hu, S.; Xue, X.; Pan, F.; Li, W.; Qi, H. Experimental and Numerical Study on the Low Velocity Impact Behavior of ABR Pipe. *Appl. Sci.* **2023**, *13*, 11390. <https://doi.org/10.3390/app132011390>

Academic Editor: Andrea Carpinteri

Received: 10 September 2023

Revised: 9 October 2023

Accepted: 12 October 2023

Published: 17 October 2023



**Copyright:** © 2023 by the authors. Licensee MDPI, Basel, Switzerland. This article is an open access article distributed under the terms and conditions of the Creative Commons Attribution (CC BY) license (<https://creativecommons.org/licenses/by/4.0/>).

## 1. Introduction

In the process of transportation, construction and operation, pipelines will be subjected to low-speed impact loads, such as collision during installation, falling stones in backfill soil, impact of foreign bodies in transportation fluid, collapse and falling rocks, etc., which will seriously affect the safety of pipeline engineering. In order to ensure the safety of pipeline engineering, the study of impact load on pipeline performance has been promoted in recent years [1], and it is necessary to study practical methods to evaluate pipeline impact resistance.

Many experiments, finite element and theoretical studies have been carried out on collision models under different conditions. Zhang et al. [2] employed the finite element method to study the deformation of oil and gas pipelines caused by rockfall impacts and explored the pipeline deformations induced by spherical and cubic rockfalls under radial, inclined, and eccentric impacts. Pichler et al. [3] proposed the motion impact model, based on the acceleration data of the rockfall impact test. Shen Wang [4] studied the impact of surface impact load on buried pipelines and proposed a method to evaluate the damage degree of buried pipelines under heavy surface impact. Rao et al. [5] calculated the effects of rockfall impact loads on pipeline deformation based on the Pasternak foundation model and the Winker foundation model, respectively. Wu and Li [6] developed a finite element model to study the interaction between partially exposed pipelines and soil under debris flow impact and analyzed the influence of factors such as debris flow velocity, impact angle, and block size on the pipelines. Yang et al. [7] used a nonlinear dynamic finite element method to simulate the process of falling objects hitting submarine pipelines, and the results show that the impact at  $90^\circ$  has the greatest influence on the plastic deformation of the

pipeline, while the friction coefficient has little influence. However, due to the dispersion of soil properties, the large error of the research results makes it difficult to apply the theory to guide the design, construction and operation of practical pipeline engineering.

In order to evaluate the mechanical properties of pipelines under low velocity impact loads, many researchers adopt the low velocity impact test method [8]. Obeid et al. [9] studied the mechanical response of a lined pipe (compound pipe) under dynamic impact with experimental and numerical investigation. A three-dimensional explicit dynamic nonlinear finite element model was proposed to evaluate the residual stress, energy dissipation and velocity of the impact process as functions of different pipes and free-fall heights. Ammar et al. [10] studied the damage evolution of pressurized hybrid composite pipe structures under impact loads with experimental and numerical investigation. Shao et al. [11] utilized an explicit dynamic program based on the Lagrangian algorithm, considering significant nonlinear deformations, to numerically simulate the impact of spherical boulders on large-diameter pipelines. Yu Wang et al. [12] studied the impact performance for ultra-light weight cement composite filled pipe-in-pipe composite structures through drop weight impact tests and numerical simulations in LS-DYNA. The influence of the outer pipe and its thickness on impact resistance and overall bending deformation of composite pipe is proposed. Jones et al. [13] conducted a large number of lateral impact tests on fully clamped steel pipes and proposed an empirical equation to predict the impact response for hollow steel pipes based on the abundant test data [14]. Thomas et al. [15] investigated experimentally the large deformations of simply supported steel pipes subjected to static indentation at the mid-span. However, there is a lack of relevant data on the impact resistance of polyvinyl chloride (PVC) pipelines in existing studies, which leaves hidden dangers for their safe operation when they are increasingly widely used.

High performance hard PVC pipe uses polyvinyl chloride polymer material, to make a new and innovative pipe for water supply and water transportation, based on traditional PVC-M pipe and PVC-U pipe [16–21]. It improves the mechanical properties of the product, and greatly improves the pipe connection mode. A PVC pipeline with its light weight, corrosion resistance, reliable connection, smooth inner wall and other advantages, in water transmission and diversion engineering, is more and more widely used [22,23]. In recent years, research on PVC pipes has focused on the material ratio and mechanical properties of pipes [24–27]. Costa et al. [28] conducted experiments to study the external strain of buried PVC pipes under local ground settlement and observed that the pipeline response increased with the increase in backfill density and the decrease in soil constraint. Lucchi and Lorenzini [29] conducted a transient analysis of the radiative heat exchange between rotating PVC pipes inside a furnace and infrared lamps using a finite element model. A critical angular velocity was proposed for the end-forming process of PVC pipes based on their findings. Ariyoshi et al. [30] conducted on-site measurements to assess the response of small PVC pipes to construction stress, traffic loads, and internal pressure. Additionally, PVC pipes excavated after 11 years of operation were tested under cyclic load. At present, there is a lack of research data on the impact resistance of PVC pipes.

Therefore, ABR pipelines based on ABR pipeline material formula improvement production is studied in this paper, and a low-speed impact test method is used to test ABR pipeline. This paper studies the impact resistance of ABR pipelines, and puts forward a calculation method to evaluate the impact failure of pipelines according to the test results, which can provide a safety evaluation method for pipeline engineering designers and construction personnel.

## 2. Experimental Specimens and Theories

### 2.1. Design of Experiment

At a temperature of  $23 \pm 1$  °C, a low velocity impact test was carried out for an ABR pipeline. Considering the influence of drop hammer weight and height on the impact resistance of a pipeline, the drop hammer weight was divided into four grades of 5.20 kg, 7.80 kg, 10.20 kg and 12.90 kg and the height of drop hammer is divided into five grades

of 0.25 m, 0.50 m, 1.00 m, 1.50 m and 2.00 m. There are 20 sets of test specimens, each consisting of three samples, as indicated in Table 1. ABR pipe with a ring stiffness grade of 1.0 Mpa, outer diameter of 630 mm and wall thickness of 20 mm was used in the test. The pipe material is isotropic and homogeneous. According to the ASTM D638-14 standard [31], the material tensile test of ABR pipes is shown in the Figure 1. The yield strength, elastic modulus and elongation at break of pipeline materials are 40.07 MPa, 3012.50 MPa and 0.60 respectively. The pipe was provided by Shandong Dongxin Plastic Technology Co., Ltd. (Liaocheng, Shandong).

**Table 1.** Parameters of specimens.

Specimen	Height (H/m)	Mass (M/kg)	Energy (E/J)	Specimen	Height (H/m)	Mass (M/kg)	Energy (E/J)
M1-H1	0.25	5.20	12.74	M3-H1	0.25	10.20	24.99
M1-H2	0.50	5.20	25.48	M3-H2	0.50	10.20	49.98
M1-H3	1.00	5.20	50.96	M3-H3	1.00	10.20	99.96
M1-H4	1.50	5.20	76.44	M3-H4	1.50	10.20	149.94
M1-H5	2.00	5.20	101.92	M3-H5	2.00	10.20	199.92
M2-H1	0.25	7.80	19.11	M4-H1	0.25	12.90	31.605
M2-H2	0.50	7.80	38.22	M4-H2	0.50	12.90	63.21
M2-H3	1.00	7.80	76.44	M4-H3	1.00	12.90	126.42
M2-H4	1.50	7.80	114.66	M4-H4	1.50	12.90	189.63
M2-H5	2.00	7.80	152.88	M4-H5	2.00	12.90	252.84

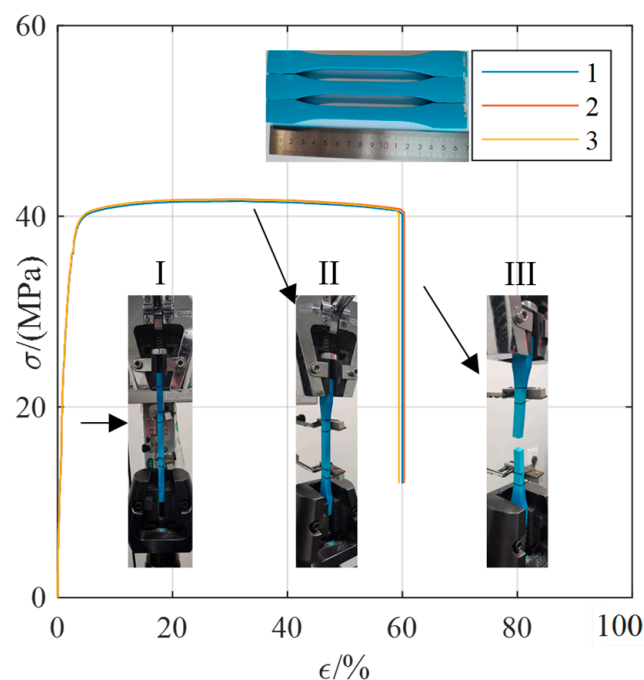


**Figure 1.** The material tensile test of ABR pipes.

## 2.2. Methods and Theories

The test system consists of a 3.2 m high bracket, steel guide rails, V-shaped fixtures, test components, drop hammer and data acquisition systems, as shown in Figure 2. According to GB/T14152-2001 [32] and ASTM D7136 [33], D90 type drop hammer with multiple quality grades and a steel V-shaped fixture with an included angle of 120° were selected for the test. The drop hammer head did not deform after repeated impacts in the test. The fixture and bracket are bolted to the ground to ensure the stability of the structure. The use of a pressure rod fixed pipeline prevented pipeline rebound. Lubricant is coated inside the guide rail to eliminate the friction effect of the inner wall of the guide rail on the drop

hammer. During the test, the drop hammer is connected with the decoupling device and pulled up to the specified height. When the drop hammer stabilizes, showing no obvious shaking, the drop hammer is released through the decoupling device to make it fall freely and impact on the axial midpoint and circumferential highest point of the specimen. An acceleration sensor is installed at the hammer head to measure the acceleration time–history curve of the falling hammer in the impact process, and the data acquisition frequency is 20 kHz. The upper frequency of the acquisition instrument is set at 800 Hz, in order to filter the influence of higher frequency signals.

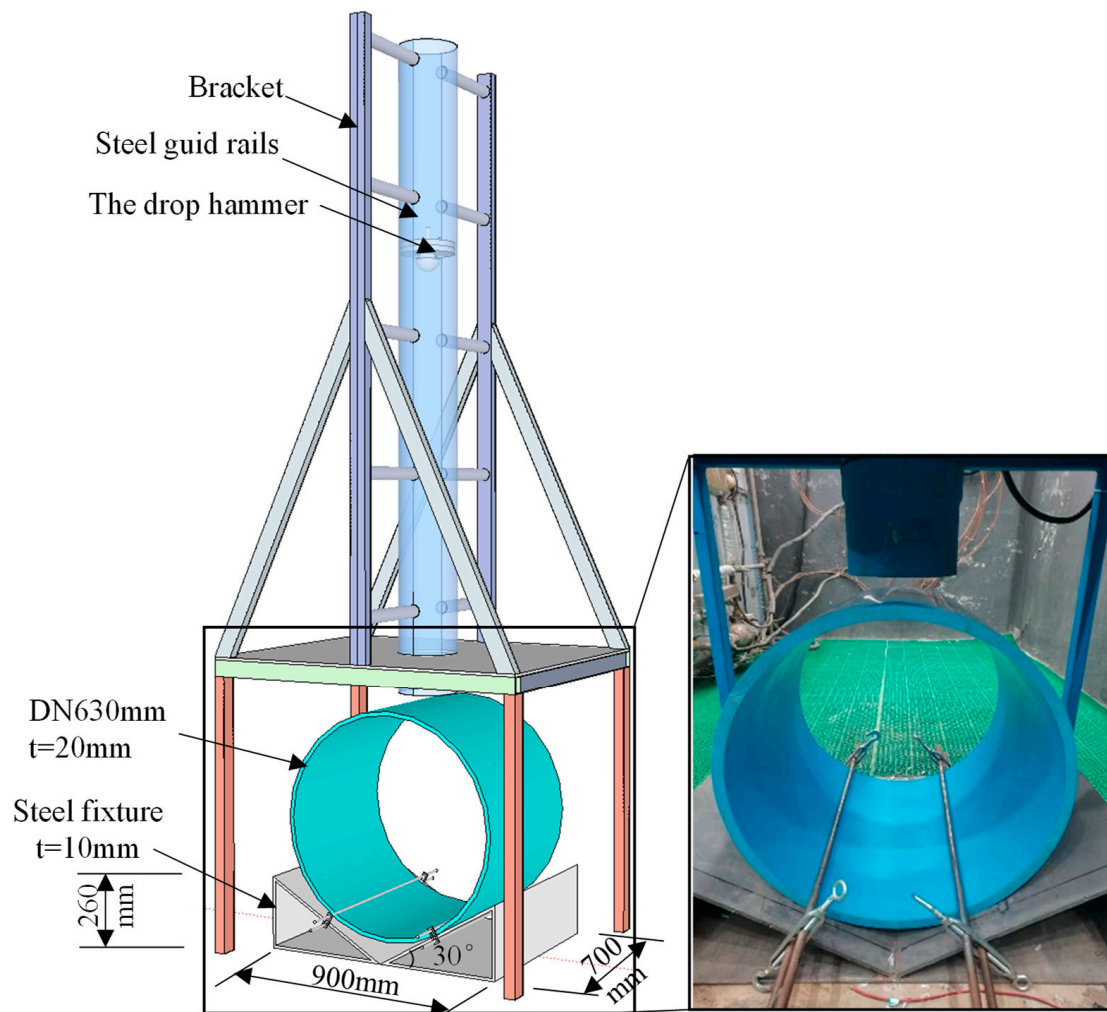


**Figure 2.** Impact test apparatus.

Using the acceleration time-history curve data collected by the test accelerometer, the impact force time-history curve is calculated according to ASTM D7136/D7136M-12 [33], and the vertical displacement of the drop hammer during the impact load can be obtained by quadratic integration of the acceleration curve. The formula is given by

$$F = ma \quad (1)$$

$$v = v_0 + gt - \int_0^t a dt \quad (2)$$

$$u = \int_0^t v dt \quad (3)$$

where  $F$  is the impact force,  $m$  is the mass of drop hammer,  $a$ ,  $v$  and  $u$  are the acceleration, velocity, displacement of drop hammer,  $v_0$  is the impactor velocity at time of initial contact,  $t$  is the time during impactor drop and impact event,  $g$  is the acceleration due to gravity.

In the initial conditions of the experiment, the height  $H$  and mass  $m$  of the falling hammer were pre-set. The initial velocity of the hammer at the moment of impact can be calculated using Formula (4). The experimental curves obtained through the tests provide temporal data  $t$  and acceleration  $a$ . At this point, Formula (1) is transformed into Formula (5). The corresponding velocity and displacement temporal data can be calculated using Formulas (6) and (7) respectively. These calculations are derived from the experimental data curves.

$$v_0 = \sqrt{2gH} \quad (4)$$

$$F_i = m a_i \quad (5)$$

$$v_i = v_0 + gt - \sum_0^i a_i \Delta t \quad (6)$$

$$u_i = \sum_0^i v_i \Delta t \quad (7)$$

where  $\Delta t$  is the time interval between experimental data collection points,  $a_i$ ,  $v_i$ ,  $u_i$ ,  $F_i$  is the acceleration, velocity, displacement, impact force at the moment of  $i * \Delta t$ .

### 3. Experimental Results and Discussion

#### 3.1. Experimental Phenomenon

In low velocity impact tests, the impact dents on the surface of the pipeline serve dual purposes. On one hand, they indicate the size of the contact area during the impact process, while on the other hand, the trend of these impact dents varies with the changing impact energy. To clearly illustrate this experimental phenomenon, photographs of the impact points on the pipeline after the initial impact of all tests were taken, as shown in Figure 3. The vertical direction in the images corresponds to the axial direction of the pipeline, while the horizontal direction represents the circumferential direction of the pipeline. Additionally, the red arc in Figure 3 outlines the boundaries of the impact marks. It is important to note that, at a drop height of 0.25 m, there were hardly any noticeable impact marks. Thus, the impact dents at this height are not presented in Figure 3.

The contact region between the hammer and the pipeline exhibits distinct frictional traces. For conditions with smaller drop heights and lower masses, the shapes of these marks are approximately elliptical and nearly circular. However, with the increase in impact energy, the area of these marks enlarges, and their shapes elongate along the axial direction of the pipeline, gradually transforming into more pronounced elliptical shapes. This phenomenon becomes more prominent with changes in height compared to variations in hammer mass. It is worth mentioning that the contact area between the hammer and the pipeline is very small in these experiments, allowing the impact load to be treated as a concentrated load at the impact point in relevant theoretical calculations, following the conventions of impact studies in similar scientific literature.

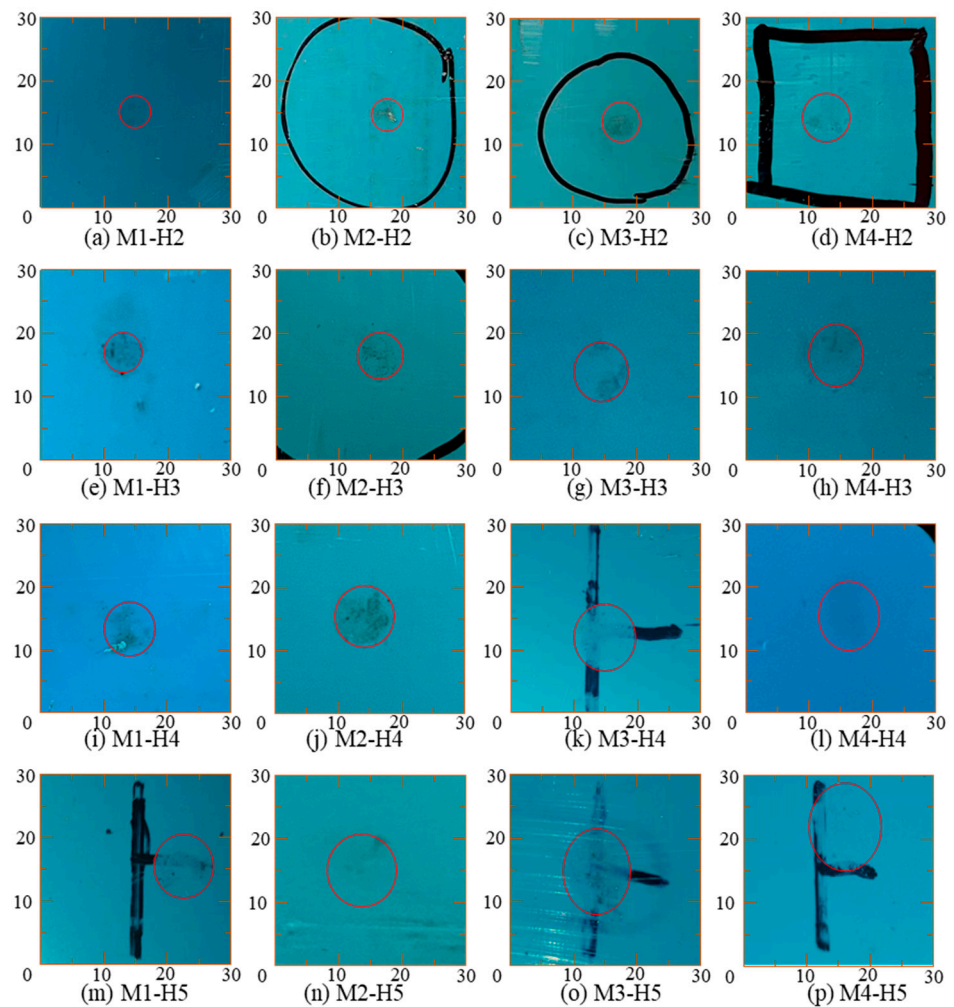


**Figure 3.** Impact dent (unit: mm).

### 3.2. History Curve

Formula (5) calculates the time-history curves of impact force for each set specimen of three samples, and takes the average, as shown in Figure 4. When the speed of the specimen accelerates from zero to close to the speed of the hammer head, the impact force intensifies. When the impact begins to reach its peak, the impact force causes the violent vibration of the specimen and the drop hammer, resulting in the rapid change of the contact area between the specimen and the drop hammer, which is manifested as the fluctuation of the impact time-history curve. After the vibration, the specimen moved down and kept close contact with the drop hammer. The displacement time-history curve was calculated according to Formulas (6) and (7), as shown in Figure 5. It is found that when the impact energy is small, the elastic deformation of the pipeline accounts for a large proportion. In the process of the first impact, with the recovery of the elastic deformation of the pipeline, the drop hammer rebounds, leading to the unloading of the impact force. As the impact energy increases, the deformation velocity of the pipeline decreases less than the impact velocity of the drop hammers due to the inertia action, resulting in no rebound phenomenon of the drop hammer in the first impact process, and the separation of the pipeline and the drop hammer occurs in the drop hammer falling process. The separation of the pipeline and the drop hammer leads to the unloading of the impact force. The second contact process between pipeline and drop hammer is not studied in this paper.

The time-history curves of specimen impact force are similar in shape, which can be divided into three stages: I—elastic stage, II—elastic-plastic stage and III—plastic

development stage. In the elastic stage, pipeline impact reaction increases linearly with impact time. In the elastic-plastic stage, the pipeline reduces the impact energy of the drop hammer through its own energy dissipation, and the tangential modulus of impact force decreases significantly, but the impact force in the contact area still increases and gradually reaches the peak value. In the plastic development stage, the material part of the pipeline enters the strengthened section after yielding, and the impact force in the contact area decreases with the increase of the pipeline deformation. The peak impact force increases with the increase of impact height at the same weight of drop hammer and the peak impact force increases with the increase of the drop hammer mass at the same height of drop hammer.

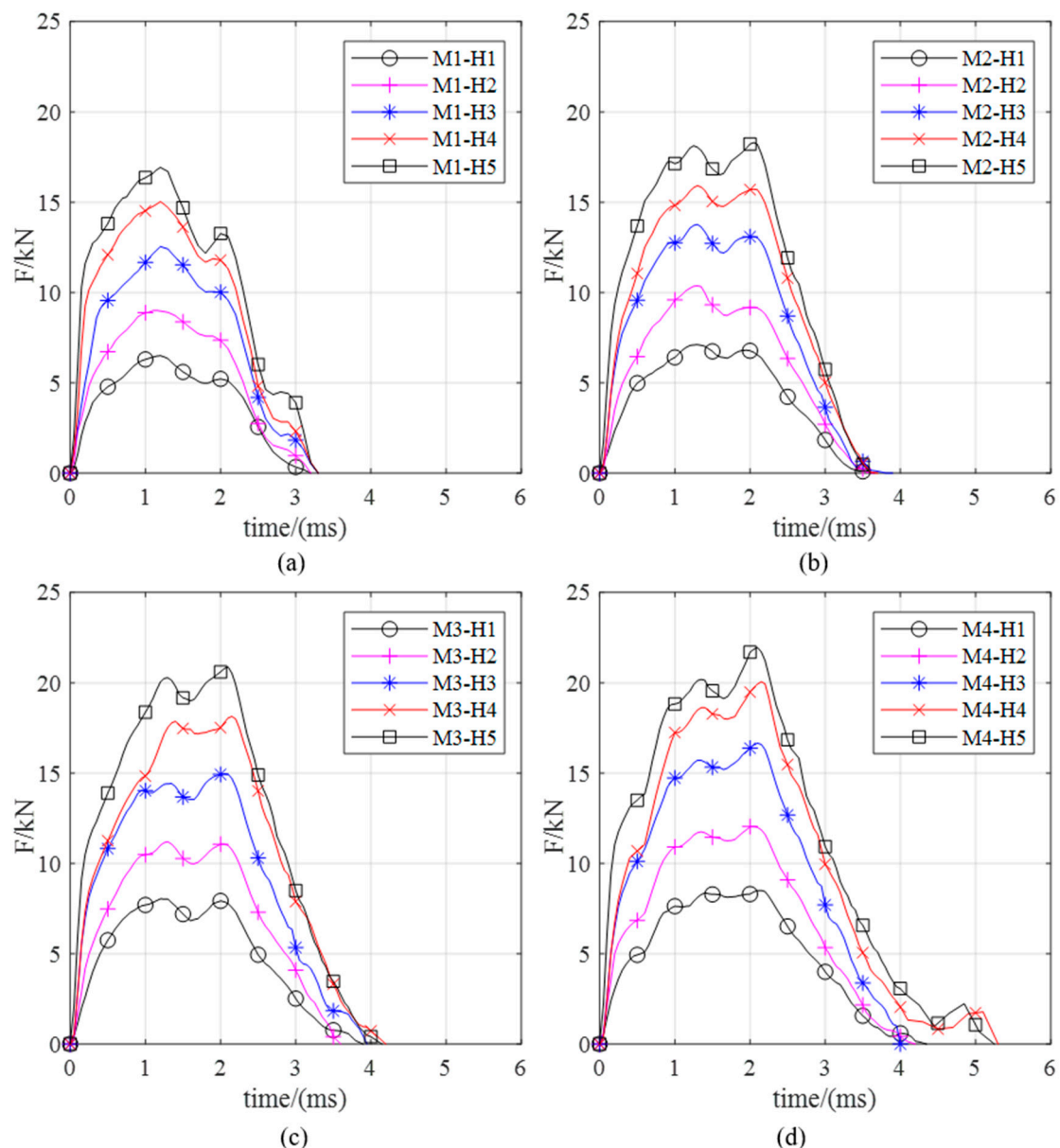


**Figure 4.** Impact-time history curves of specimens. (a) The impact-time history curves of  $m = 5.20$  kg; (b) The impact-time history curves of  $m = 7.80$  kg; (c) The impact-time history curves of  $m = 10.20$  kg; (d) The impact-time history curves of  $m = 12.90$  kg.

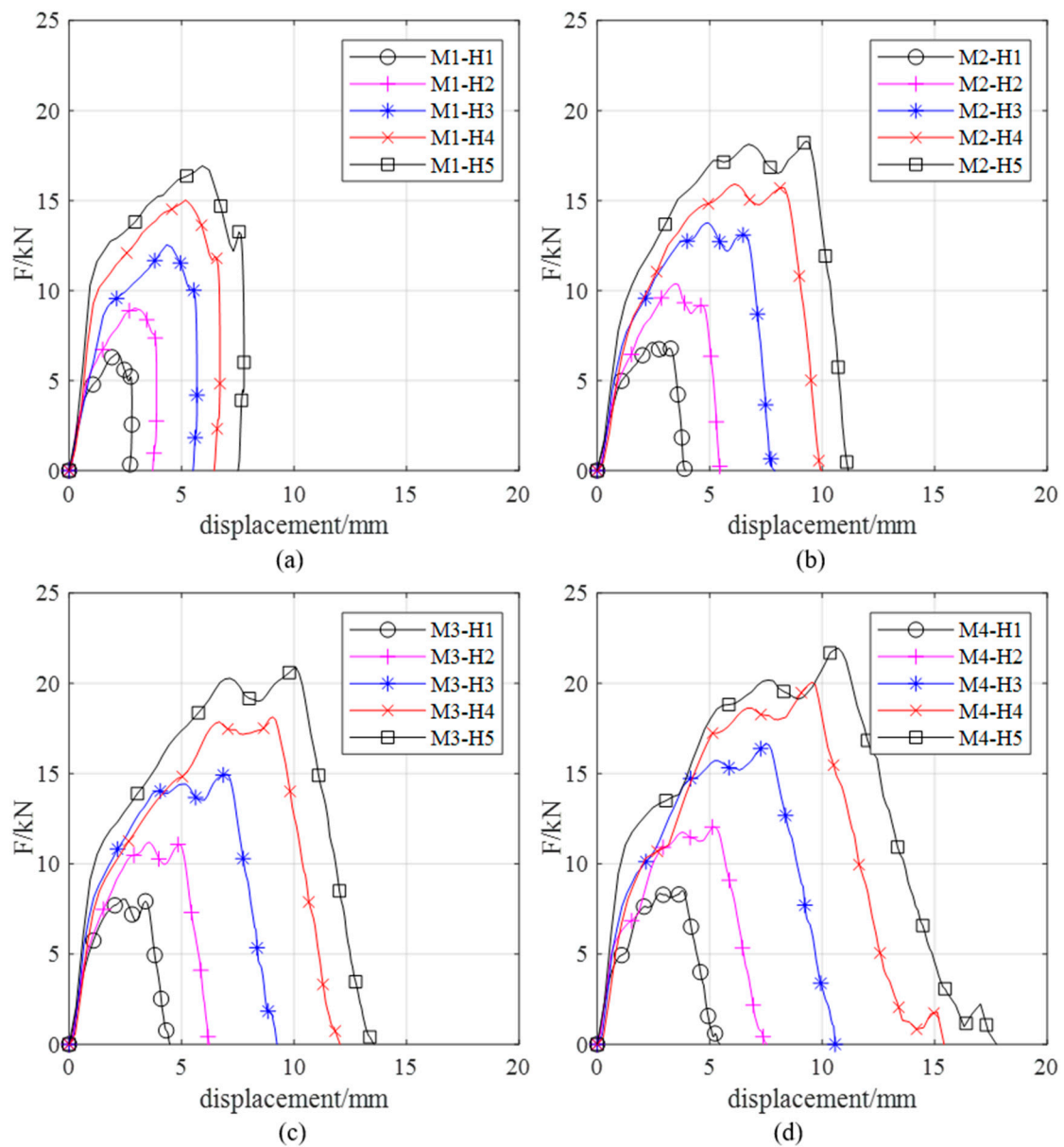


**Figure 5.** Impact-displacement history curves of specimens. (a) The impact- displacement history curves of  $m = 5.20$  kg; (b) The impact- displacement history curves of  $m = 7.80$  kg; (c) The impact- displacement history curves of  $m = 10.20$  kg; (d) The impact- displacement history curves of  $m = 12.90$  kg.

### 3.3. Energy Dissipation Capacity

To evaluate the energy dissipation capacity of pipelines in the process of falling hammer impact, Reid [34] proposed a calculation Formula (8) for the energy dissipation capacity of metal pipelines, and believed that the energy dissipation capacity of metal pipelines in the process of impact was related to the mass per unit length of pipelines and the maximum displacement of pipelines.

$$E_{sa} = \frac{E_a}{W\delta_a} \tag{8}$$

where  $E_{sa}$  is the energy dissipation coefficient of the pipeline,  $E_a$  is the energy absorbed by the pipeline,  $W$  is the mass per unit length of the pipeline,  $\delta_a$  is the maximum displacement of the pipeline.

The energy consumed  $E_a$  is obtained by integrating the force–displacement curve, as shown in Formula (9).

$$E_a = \int_0^{T_s} F(t)w(t)dt \tag{9}$$

where  $T_s$  is the contact duration (total duration of the impact event).

In this paper, the pipe length is less than 1 m, so when calculating the energy consumption of the pipe, the mass of the specimen is used instead of the mass of the unit length of the pipe, to quantitatively evaluate the energy consumption capacity of the structure under impact force. The calculation results are shown in Table 2. In the process of impact, energy loss includes kinetic energy loss of drop weight, potential energy loss of drop weight, heat energy loss and sound energy loss generated by impact. Relevant studies show that the loss of heat and sound energy generated by impact is less than 5%, and the impact of this loss on the results will be ignored in this paper.

**Table 2.** The energy absorption capacity of specimens.

Specimen	$W\delta_a$	$E_a$	$E_{sa}$	Specimen	$W\delta_a$	$E_a$	$E_{sa}$
M1-H1	12.876	0.136	93.749	M3-H1	0.448	24.578	54.844
M1-H2	25.670	0.190	134.284	M3-H2	0.623	48.784	78.310
M1-H3	51.241	0.281	181.429	M3-H3	0.924	97.152	105.171
M1-H4	76.769	0.329	231.982	M3-H4	1.204	145.464	120.832
M1-H5	102.303	0.383	265.241	M3-H5	1.355	193.481	142.792
M2-H1	19.409	0.299	64.109	M4-H1	0.689	29.941	43.466
M2-H2	38.640	0.420	91.273	M4-H2	0.954	59.398	62.282
M2-H3	77.044	0.604	126.241	M4-H3	1.337	117.688	88.013
M2-H4	115.423	0.763	149.109	M4-H4	1.949	177.120	90.858
M2-H5	153.733	0.853	177.975	M4-H5	2.244	234.843	104.673

The mechanical energy loss of the drop hammer is transformed into the strain energy of the structure after absorption by the pipe. The elastic strain energy is dissipated by the deformation and recovery of the material, and the plastic strain energy is released by the irreversible deformation of the material. The data show that the absorption energy and energy dissipation coefficient of pipeline increase with the increase of drop hammer height under the same mass grade. At the same height, the absorbed energy increases with the increase of mass, and the energy dissipation coefficient decreases with the increase of mass. The  $E_{sa}$  of specimens is more than 40 in the process of impact. With the increase of the impact energy level, the plastic deformation area of the pipe increases, leading to the improvement of the energy absorption coefficient of the specimen.

### 3.4. Impact Force

In the whole impact process, various parameters will affect the impact force. In this study, for all specimens, the hammer head shape of the drop hammer, the boundary conditions of the specimens and the materials of the specimens are the same. Therefore, only the geometric parameters of the specimen, the weight of the drop weight and the height of the drop weight can significantly affect the peak impact force. The peak impact force of each specimen was extracted according to the impact time curve, as shown in Table 3. This paper will use a dimensional analysis method to analyze the peak impact force obtained from the test. The dimensional harmony principle as the basic principle of dimensional analysis, also called dimensional consistency principle or the principle of dimensional homogeneity, describes the relationship between complete physical equations in both their differential and integral forms. Its various dimensions must be consistent, that is only two types of the same physical quantity for addition and subtraction.

In the analysis process of this paper, we choose the falling weight ( $m$ , dimension  $[M]$ ), the initial impact velocity ( $v_0$ , dimension  $[L][T]^{-1}$ ), the ring stiffness ( $S_p$ ,  $[M][T]^{-2}$ ), peak impact force ( $F_{max}$ , dimension  $[M][L][T]^{-2}$ ), pipe quality ( $m_2$ , The dimension  $[M]$ ) as

the basic physical quantities. It is assumed that basic physical quantities meet physical equations, as shown in Formula (10), and their unit relations are shown in Formula (12).

$$f(m, v_0, S_p, F_{\max}, m_2) = 0 \tag{10}$$

$$m^{y_1} \cdot v_0^{y_2} \cdot S_p^{y_3} \cdot F_{\max}^{y_4} \cdot m_2^{y_5} = 0 \tag{11}$$

$$[M]^{y_1+y_4+y_5} \cdot [L]^{y_2+y_4} \cdot [T]^{-y_2-2y_3-2y_4} = 0 \tag{12}$$

The dimensional matrix of the equation is:

$$\begin{bmatrix} 1 & 0 & 1 & 1 & 1 \\ 0 & 1 & 0 & 1 & 0 \\ 0 & -1 & -2 & -2 & 0 \end{bmatrix}$$

The basic solution of the linear homogeneous system is:

$$\begin{bmatrix} -\frac{1}{2} & -1 & -\frac{1}{2} & 1 & 0 \\ -1 & 0 & 0 & 0 & 1 \end{bmatrix}^T$$

Five physical quantities, involving three basic dimensions, are selected for the process of low velocity impact. This physical and mechanical process can be described by two dimensionless relations.

$$F(\pi) = 0 \tag{13}$$

$$\pi_1 = m^{-\frac{1}{2}} \cdot v_0^{-1} \cdot S_p^{-\frac{1}{2}} \cdot F_{\max}^1 \tag{14}$$

$$\pi_2 = m^{-1} \cdot m_2^1 \tag{15}$$

According to Formula (14), the function relation Formula (16) of peak load can be rewritten:

$$F_{\max} = \frac{1}{\pi_1} \cdot \sqrt{m} \cdot v_0 \cdot \sqrt{S_p} \tag{16}$$

The constant  $\pi_1$  has some corresponding relation with  $\pi_2$  and is related to  $m_1$  and  $m_2$ . By introducing the relation  $\varphi$ , Formulas (15) and (16) are transformed into Formula (17).

$$F_{\max} = \varphi\left(\frac{m_2}{m}\right) \cdot \sqrt{m} \cdot v_0 \cdot \sqrt{S_p} \tag{17}$$

The expression of impact coefficient  $\varphi$  is supposed as the Formula (18), where a and b are undetermined constants.

$$\varphi\left(\frac{m_2}{m}\right) = a \cdot e^{b \cdot \frac{m_2}{m}} \tag{18}$$

Peak loads of 20 sets of specimens were used for fitting, as shown in Figure 6. The calculation formula of the peak load is obtained according to the fitting situation, as shown in Formula (19).

$$F_{\max} = \varphi \cdot \sqrt{m} \cdot v_0 \cdot \sqrt{S_p} \tag{19}$$

The impact coefficient  $\varphi = 10.092 \cdot e^{0.049 \cdot \frac{m_2}{m}}$ . The comparison between the peak load calculated by the formula and the test results is shown in Table 3. The results are in good agreement with the test results, with a deviation of 4.0%. It proves that the Formula (19) can provide a convenient and accurate calculation method of peak impact load for test prediction and construction safety.

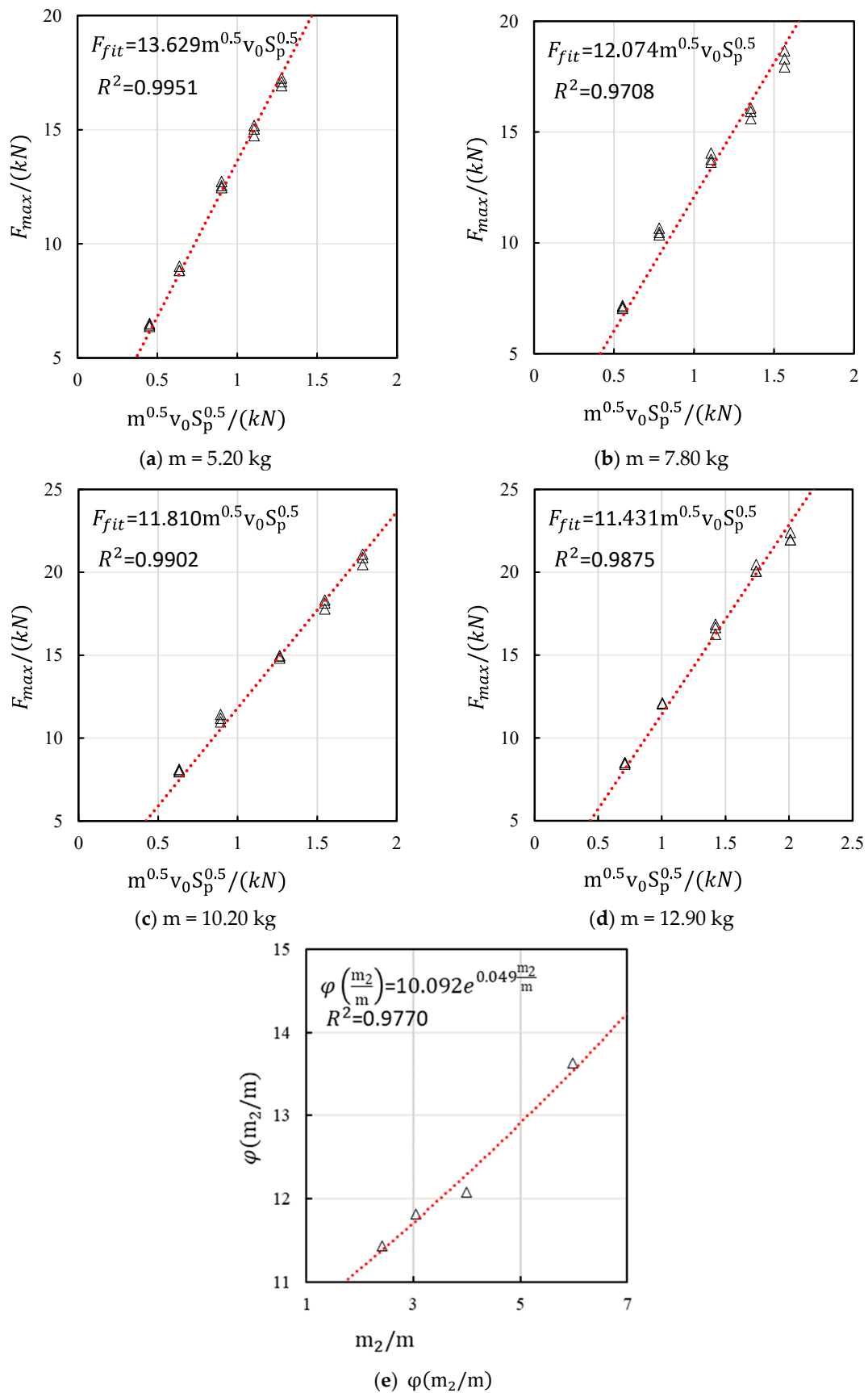


Figure 6. Peak load fitting of specimen impact process.

**Table 3.** The  $F_{max}$  and  $F_{fit}$  of specimens.

Specimen	$v$	$S_p$	$m_2$	$F_{max}$			$F_{fit}$	$F_{fit}/F_{max}$		
				1	2	3		1	2	3
M1-H1	2.214	0.008	31.122	6.505	6.375	6.440	6.110	0.939	0.958	0.949
M1-H2	3.130	0.008	31.122	9.011	8.831	8.831	8.638	0.959	0.978	0.978
M1-H3	4.427	0.008	31.122	12.545	12.730	12.460	12.218	0.974	0.960	0.981
M1-H4	5.422	0.008	31.122	15.031	15.181	14.730	14.964	0.996	0.986	1.016
M1-H5	6.261	0.008	31.122	16.924	17.093	17.262	17.279	1.021	1.011	1.001
M2-H1	2.214	0.008	31.122	7.109	7.038	7.180	6.787	0.955	0.964	0.945
M2-H2	3.130	0.008	31.122	10.368	10.472	10.660	9.595	0.925	0.916	0.900
M2-H3	4.427	0.008	31.122	13.770	13.632	14.045	13.570	0.985	0.995	0.966
M2-H4	5.422	0.008	31.122	15.914	16.073	15.596	16.620	1.044	1.034	1.066
M2-H5	6.261	0.008	31.122	18.301	17.935	18.667	19.192	1.049	1.070	1.028
M3-H1	2.214	0.008	31.122	8.037	8.117	7.957	7.412	0.922	0.913	0.932
M3-H2	3.130	0.008	31.122	11.197	10.973	11.421	10.478	0.936	0.955	0.917
M3-H3	4.427	0.008	31.122	14.958	14.958	14.808	14.820	0.991	0.991	1.001
M3-H4	5.422	0.008	31.122	18.138	17.775	18.319	18.151	1.001	1.021	0.991
M3-H5	6.261	0.008	31.122	20.877	20.459	21.086	20.960	1.004	1.024	0.994
M4-H1	2.214	0.008	31.122	8.505	8.420	8.515	8.079	0.950	0.959	0.949
M4-H2	3.130	0.008	31.122	12.048	12.068	12.118	11.421	0.948	0.946	0.942
M4-H3	4.427	0.008	31.122	16.657	16.857	16.257	16.154	0.970	0.958	0.994
M4-H4	5.422	0.008	31.122	20.056	20.056	20.457	19.784	0.986	0.986	0.967
M4-H5	6.261	0.008	31.122	21.954	21.954	22.393	22.846	1.041	1.041	1.020
Mean value									0.980	
Std. dev.									0.040	

## 4. Numerical Modeling

### 4.1. Finite Element Model

The finite element analysis model of drop hammer impact pipeline is established and calculated in ABAQUS Explicit [35]. The schematic diagram of the finite element model is shown in Figure 7. Since the drop hammer in the test can be regarded as an object that cannot be deformed at the time, the drop hammer can be set as a rigid body and simplified to a reference point, on which the initial impact velocity can be defined by using the velocity field. The mesh density affects the accuracy of the finite element model calculation. In general, the larger the mesh density, the closer the result of the model calculation will be to the real value. In this paper, the mesh size of the model is 10 mm, and the mesh subdivision size of the impact contact area is 2.0 mm. The finite element model of the specimen has a total of 646,136 units. The element shape selection criteria was employed to assess the finite element mesh. The criteria used for evaluating the elements included a geometric deviation factor greater than 0.2, edge shorter than 0.01, edge longer than 1, and stable time increment less than  $1 \times 10^{-5}$ . Additionally, the analysis errors were found to be 0 (0%), with no warnings reported. Dynamic face-surface contact is adopted between the hammer head and pipe, normal hard contact, tangential friction coefficient is defined as 0.3 by penalty function, which can properly simulate the sliding contact problem and output contact force at the same time. Other contacts are defined as normal hard contact and tangential friction contact by general contact. In the model, the drop hammer and constraint bars adopt a rigid body element, and the pipe and base adopt a C3D8 solid element. General elastic–perfectly plastic constitutive model was adopted by the pipeline and steel. The constitutive curve of ABR pipe is shown in the Figure 8. The elastic modulus and yield strength of steel fixture and steel bar are 206,000 MPa and 235 MPa respectively. As the research content in this paper is the process of low-speed movement, the strain rate effect is not considered in the material constitutive model. Richardson et al. [36] proposed the strain rate effect remains negligible if the initial impact velocity is less than 10 m/s. All specimens in this study have an initial velocity that remains below 7 m/s. The comparison between the numerical analysis and the experimental is reported in the subsequent section.

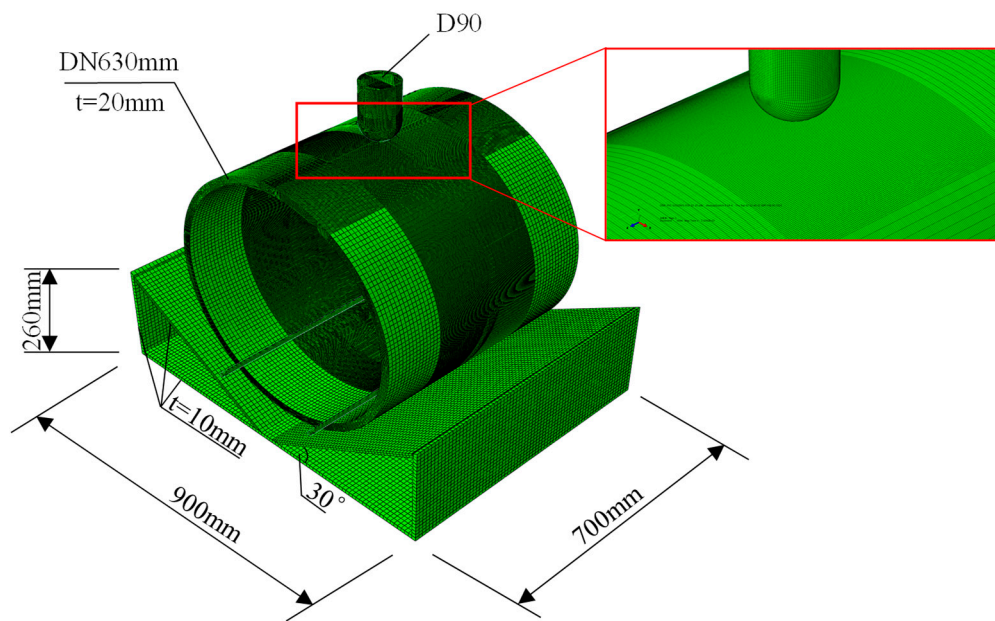


Figure 7. Finite element model of ABR.

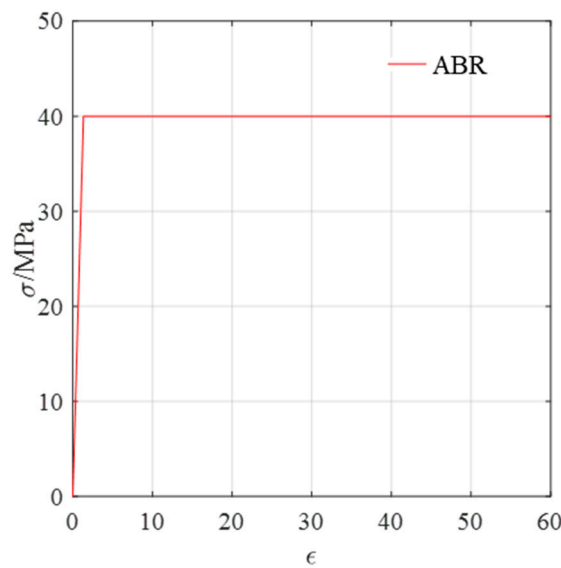


Figure 8. The material constitutive of ABR pipes.

#### 4.2. Validation of the FEM Analysis

Figure 9 shows the comparison between the finite element simulation time-history curve results of impact force and the test results of some ABR pipe specimens after impact. It can be seen from the figure that the time-history curve of impact force obtained by finite element simulation of the specimen is in good agreement with the test results. At the end of the finite element calculation, the time-history curve of impact force is slightly different from the test. The pipe specimen experienced extremely violent and rapid vibration during the impact test, and the finite element model under ideal boundary conditions could not restore the boundary condition changes during the test. At the same time, there is a certain error between the impact time and the experiment in the finite element simulation results. To verify the correctness of the finite element model in one step, the comparison of pipeline impact resistance performance indexes is given in Table 4, including peak impact force, impact time and peak displacement of the drop hammer. The deviations of peak impact force and impact time between the finite element calculation results and the average values

of the test results are 2.3% and 6.9%, respectively. The data show that the peak value of the impact reaction force increases with the increase of the drop weight, and the variation trend is consistent with the test results. The finite element can effectively analyze the failure mode of the pipeline under the impact of the falling hammer.

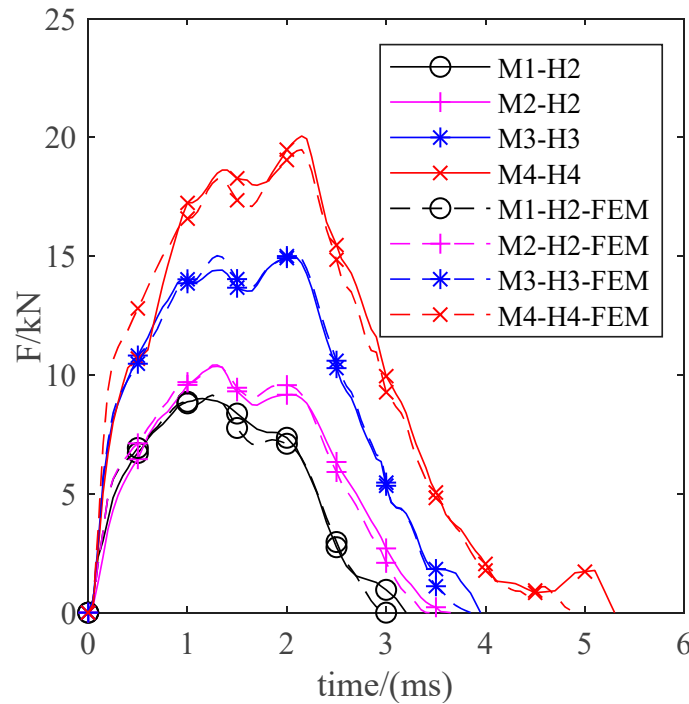


Figure 9. Comparison between the test and the FEM results.

Table 4. Summary of simulation results.

Specimen	$F_{max}$		$T_s$		Specimen	$F_{max}$		$T_s$	
	FE(kN)	FE/Test	FE(ms)	FE/Test		FE(kN)	FE/Test	FE(ms)	FE/Test
M1-H1	6.448	1.001	3.05	0.953	M3-H1	7.917	0.985	3.80	0.974
M1-H2	9.151	1.029	3.00	0.938	M3-H2	11.094	0.991	3.75	1.042
M1-H3	12.660	1.006	3.00	0.909	M3-H3	15.108	1.013	3.85	0.975
M1-H4	15.059	1.005	3.00	0.909	M3-H4	18.172	1.005	3.95	0.940
M1-H5	17.051	0.998	3.00	0.909	M3-H5	20.486	0.985	4.10	0.988
M2-H1	7.371	1.037	3.45	0.945	M4-H1	8.534	1.006	4.30	0.989
M2-H2	10.423	0.993	3.45	0.945	M4-H2	11.918	0.987	4.30	1.024
M2-H3	14.261	1.032	3.45	0.885	M4-H3	16.324	0.984	4.80	1.200
M2-H4	16.849	1.062	3.45	0.932	M4-H4	19.486	0.965	4.85	0.915
M2-H5	18.890	1.032	3.55	0.986	M4-H5	22.017	0.996	4.85	0.924
Mean value							1.006		0.964
Std. dev.							0.023		0.069

### 4.3. Failure Model of Pipes

Figure 9 shows the Mises stress nephogram of specimen M1-H1, for low impact energy. At the moment of initial contact between the drop hammer and the specimen, the impact force increases rapidly, the stress transfer speed is fast along the axial direction, the stress area is oval, and the surface of the top of the tube suffers local depression. In the process after 1.80 ms as shown in Figure 10a, the specimen and the drop hammer fall synchronously, the kinetic energy of the drop hammer decreases, the kinetic energy of the specimen increases, and the velocity of stress transfer along the circumferential direction increases. Starting from 2.5 ms, with the continuous transmission of stress in the contact

area, the stress area on the top surface of the pipe gradually extends lengthwise, and the stress in the contact area of the pipe decreases when the drop hammer falls. Until the drop hammer springs back and disconnects from the pipe at the moment of 3.05 ms, the stress on the top surface of the pipe is striped, as shown in Figure 10b.

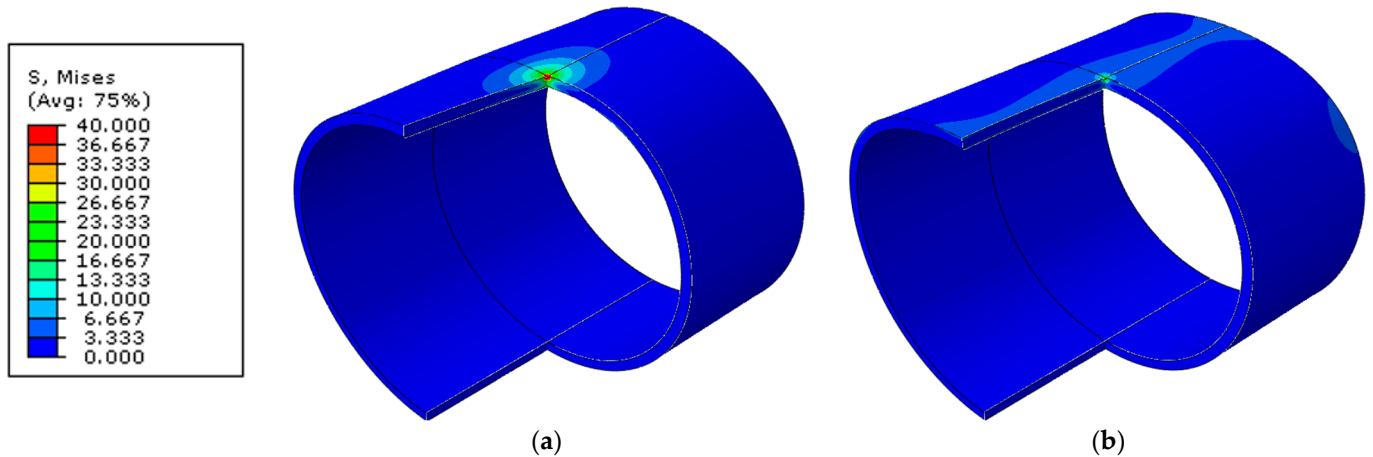


**Figure 10.** The Mises nephogram of M1-H1. (a)  $t = 1.80$  ms (b)  $t = 3.05$  ms.

With the increase of impact energy, the stress concentration area on the surface of the pipe top expands and the yield area of the pipe increases. The deformation velocity of the specimen impact contact area is greater than the falling speed of the drop hammer. After the specimen is separated from the drop hammer, the drop hammer will keep the falling speed moving for a distance, and the first impact process of the drop hammer ends at that point. In the subsequent process, the elastic strain of the specimen gradually recovered, the deformation in the contact area of the specimen first increased and then decreased, and it contacted the drop hammer again. In the subsequent process, the pipe and the drop hammer deformed synchronously until the drop hammer bounced back and separated from the specimen.

Figure 11 shows the Von Mises nephogram of specimen M4-H5, for small impact energy. The impact force increases rapidly at the initial contact moment of the drop hammer with the specimen, and local depression appears on the surface of the tube top and rapidly expands to the surrounding area. When the time reaches 1.35 ms as shown in Figure 11a, the overall surface of the top of the tube moves downward with the impact process. During the subsequent process, the specimen descends synchronously with the drop weight. At 2.15 ms, with the continuous transfer of stress in the contact area, the development of pipeline stress reached its limit, and the impact reaction force of specimen reached its peak. In the subsequent process, however, the drop hammer and the impact area of the pipe will move downward. With the dissipation of energy and the transfer of stress, the stress on the top surface of the pipe gradually decreases, which is manifested as the unloading of the impact time-history curve. Until the drop hammer disconnects from the pipe, as shown in Figure 11b, the pipe stress is distributed in a strip type, and a large stress area appears at the top and waist of the pipe.

By comparison, it can be found that the specimen is subjected to a great deal of impact energy at the moment of impact, the strain is obviously transferred in the circumferential direction, and the strain peak appears later in the position far from the impact contact point than in the nearer position. The finite element results show that the failure modes of all specimens under impact load are similar, and all specimens are bent in local depressions.

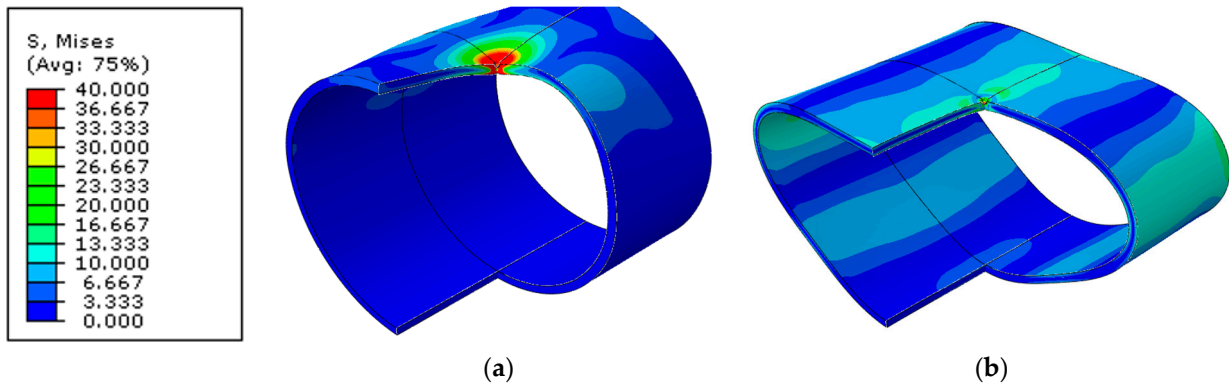


Figure 11. The Von Mises nephogram of M4-H5. (a)  $t = 1.35$  ms (b)  $t = 4.85$  ms.

4.4. Strain Analysis

The circumferential and axial strains in the pipeline impact contact area were selected for comparative analysis, as shown in Figures 12 and 13. Plastic regions appear on the outer surface of the contact area of the top of the pipe, and plastic regions appear on the inner surface of the contact area of the top of the pipe. With the increase of the weight and height of the drop hammer, the plastic regions on the outer surface of the top of the pipe increase. There is no plastic strain appearing on the inner surface of the contact area of the tube top of specimens with a height of 0.25 m and 0.5 m. For the specimens with a height of 1.0 m, no plastic strain appeared on the inner surface of the contact area of the tube top of M1-H3, while plastic strain appeared on the inner surface of the contact area of the tube top of other specimens. Plastic strain appeared on the inner surface of the contact area of the tube top of specimens with heights of 1.5 m and 2.0 m.

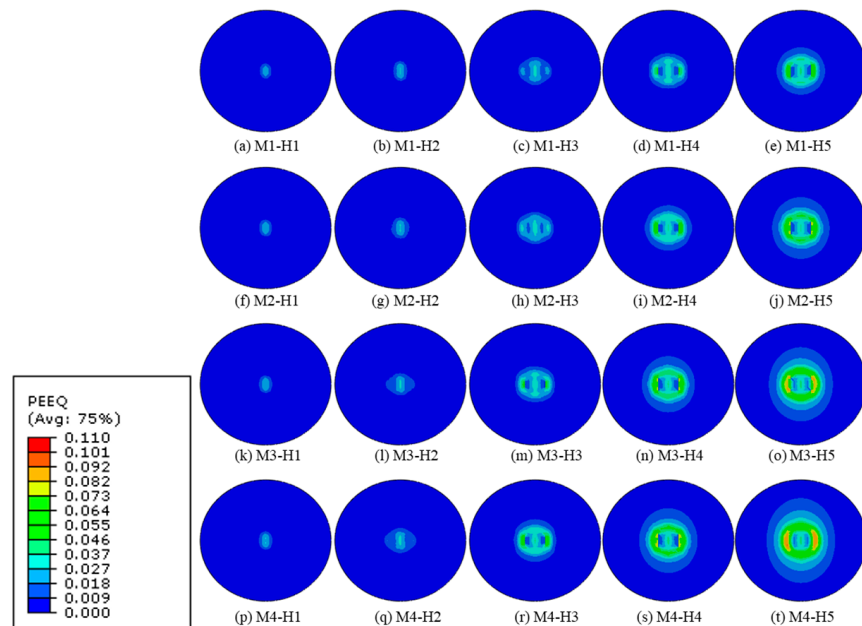
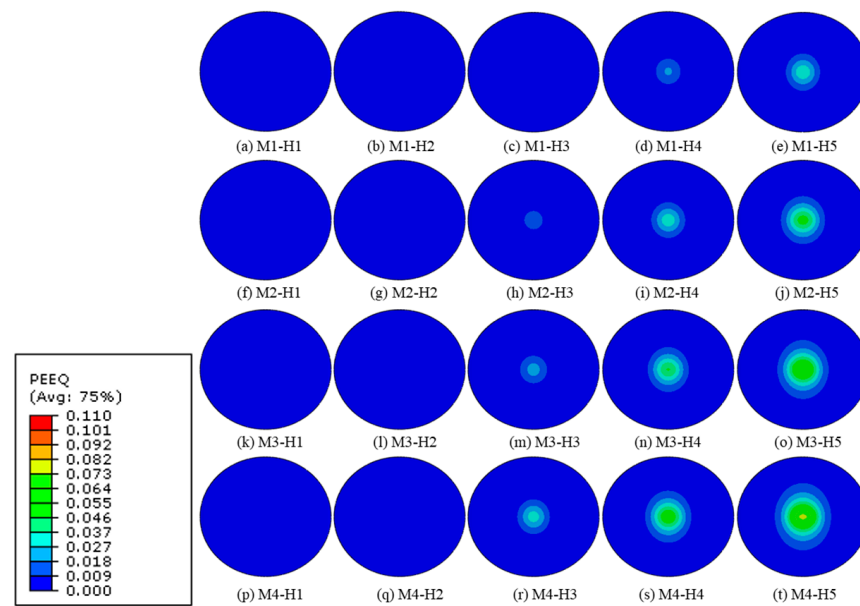


Figure 12. PEEQ nephogram of the outer surface of the contact area.



**Figure 13.** PEEQ nephogram of the inner surface of the contact area.

The impact of the drop hammer on the pipeline caused great damage to the contact part and the local area around it. When the impact energy level is small, the impact energy is transmitted along the axial, longitudinal and circumferential directions of the pipeline, and gradually transferred to the foundation or dissipated by the vibration of the pipeline itself. Thanks to the good ductility of ABR material, the plastic area produced by the pipeline is small, and the inside of the pipeline in the impact contact area is not damaged. With the increase of impact energy level, the damage in the contact area develops rapidly in the longitudinal and circumferential directions, and develops to the inside of the pipe, and the plastic area gradually develops to the inner surface of the pipe.

## 5. Discussion

In this paper, the impact of drop weight quality and height on the impact resistance of ABR pipeline in the low-speed impact process is studied, but there are still some contents that have not been fully studied, such as the following contents:

- (1) The impact of pipeline geometry characteristics such as wall thickness, diameter, and pipe length on the pipeline's impact resistance has not been thoroughly examined.
- (2) The effects of impact angle and drop hammer shape on the pipeline's impact resistance have not been deeply studied.
- (3) Our study was limited to ABR pipes of the same material, neglecting the significant impact that different polymer ABR material formulations can have on the material's mechanical properties.
- (4) We have yet to delve into the critical load leading to pipeline failure and the underlying mechanisms.

## 6. Summary and Conclusions

In this paper, 20 low-speed impact tests of ABR pipeline were carried out by using a drop hammer device. Combined with finite element numerical simulation, the dynamic response law of different drop hammer mass and height on pipeline impact was studied.

The following main conclusions can be drawn:

- (1) The contact region displayed distinct frictional traces, with marks transitioning from elliptical to pronounced elliptical shapes as impact energy increased.

- (2) In this paper, through the quantitative calculation of the energy dissipation coefficient of the ABR specimen, it is proved that the energy dissipation capacity of ABR pipe is good, which can fully dissipate the impact energy.
- (3) Based on the test results and dimensional analysis method, a calculation method suitable for calculating the peak impact force in the first drop hammer impact process of the pipeline is proposed, which can provide a simple calculation method for ensuring pipeline safety.
- (4) Obvious plastic deformation occurs in the pipeline during low speed impact, and the failure mode of the pipeline is that the local plastic strain develops too much.
- (5) The numerical model can well predict the time-history change of impact force and pipeline strain development process in a low-speed impact process.

**Author Contributions:** Conceptualization, S.H., C.S. and X.X.; methodology, S.H. and C.S.; software, S.H., C.S. and X.X.; validation, S.H., C.S., F.P. and W.L.; formal analysis, C.S. and X.X.; investigation, H.Q.; resources, F.P.; data curation, S.H. and C.S.; writing—original draft preparation, S.H. and C.S.; writing—review and editing, W.L. and S.H.; visualization, S.H., C.S. and X.X.; supervision, S.H. and C.S.; project administration, S.H. and C.S.; funding acquisition, S.H. and F.P. All authors have read and agreed to the published version of the manuscript.

**Funding:** This research was funded by the Innovation Group Science Foundation of the Natural Science Foundation of Chongqing, China (cstc2020jcyj-cxttX0003), the National Natural Science Foundation of China (51739008), the Key Program of the National Science Foundation of China (52130901) and the Taishan Industry Lead-ing Talent Project Special Fund.

**Institutional Review Board Statement:** Not applicable.

**Informed Consent Statement:** Not applicable.

**Data Availability Statement:** Experimental data and numerical models in the study are available from the corresponding author upon reasonable request.

**Conflicts of Interest:** The authors declare no conflict of interest.

## Nomenclature

$Pa$	the acceleration of drop hammer
$E$	the energy of drop hammer at initial time
$E_a$	the energy absorbed by the pipeline
$E_{sa}$	the energy dissipation coefficient of the pipeline
$e$	the napierian logarithm
$F$	the impact force
$F_{max}$	the peak impact force in experiment
$F_{fit}$	the peak impact force according to the Formula (13)
$g$	the acceleration due to gravity
$H$	the height of drop hammer
$m$	the mass of drop hammer
$m_2$	the mass of specimen
$S_p$	the ring stiffness of specimen
$T_s$	the contact duration (total duration of the impact event)
$t$	the time during impactor drop and impact event
$\Delta t$	the time interval between experimental data collection points
$u$	the displacement of drop hammer
$v$	the velocity of drop hammer
$v_0$	the impactor velocity at time of initial contact
$W$	the mass per unit length of the pipeline
$\delta_a$	the maximum displacement of the pipeline
$\varphi$	the impact coefficient

## References

1. Zeinoddini, M.; Arabzadeh, H.; Ezzati, M.; Parke, G. Response of submarine pipelines to impacts from dropped objects: Bed flexibility effects. *Int. J. Impact Eng.* **2013**, *62*, 129–141. [[CrossRef](#)]
2. Zhang, J.; Liang, Z.; Han, C.J. Failure Analysis and Finite Element Simulation of Above Ground Oil–Gas Pipeline Impacted by Rockfall. *J. Fail. Anal. Prev.* **2014**, *14*, 530–536. [[CrossRef](#)]
3. Pichler, B.; Hellmich, C.; Mang, H. Impact of rocks onto gravel Design and evaluation of experiments. *Int. J. Impact Eng.* **2005**, *31*, 559–578. [[CrossRef](#)]
4. Wang, S. Evaluation of underground pipe-structure interface for surface impact load. *Nucl. Eng. Des.* **2017**, *317*, 59–68. [[CrossRef](#)]
5. Rao, P.; Wu, Z.; Cui, J. Analysis of Deformation of Adjacent Buried Pipeline Under Rockfall Impact Load. *Geotech. Geol. Eng.* **2022**, *40*, 1463–1474. [[CrossRef](#)]
6. Wu, Y.; Li, J. Finite element analysis on mechanical behavior of semi-exposed pipeline subjected to debris flows. *Eng. Fail. Anal.* **2019**, *105*, 781–797. [[CrossRef](#)]
7. Yang, X.-J.; Tan, T.; Xiu, Z.-X.; Yan, X.-Z.; Feng, Y.-X. Elastic-plastic finite element analysis of submarine pipeline impacted by dropped objects. *Eng. Mech.* **2011**, *6*, 189–194.
8. Espinosa, H.; Dwivedi, S.; Lu, H.-C. Modeling impact induced delamination of woven fiber reinforced composites with contact/cohesive laws. *Comput. Methods Appl. Mech. Eng.* **2000**, *183*, 259–290. [[CrossRef](#)]
9. Obeid, O.; Alfano, G.; Bahai, H.; Jouhara, H. Mechanical response of a lined pipe under dynamic impact. *Eng. Fail. Anal.* **2018**, *88*, 35–53. [[CrossRef](#)]
10. Maziz, A.; Tarfaoui, M.; Gemi, L.; Rechak, S.; Nachtane, M. A progressive damage model for pressurized filament-wound hybrid composite pipe under low-velocity impact. *Compos. Struct.* **2021**, *276*, 114520. [[CrossRef](#)]
11. Shao, B.; Yan, Y.; Wang, X.; Yan, X. Dynamics and strain-based design of the large-diameter pipe under the impact of a falling rock. *IOP Conf. Ser. Mater. Sci. Eng.* **2020**, *738*, 012010. [[CrossRef](#)]
12. Wang, Y.; Qian, X.; Liew, J.R.; Zhang, M.-H. Experimental behavior of cement filled pipe-in-pipe composite structures under transverse impact. *Int. J. Impact Eng.* **2014**, *72*, 1–16. [[CrossRef](#)]
13. Jones, N.; Birch, S.E.; Birch, R.S.; Zhu, L.; Brown, M. An experimental study on the lateral impact of fully clamped mild steel pipes. *Proc. Inst. Mech. Eng. Part E J. Process. Mech. Eng.* **1992**, *206*, 111–127. [[CrossRef](#)]
14. Jones, N.; Shen, W.Q. A theoretical study of the lateral impact of fully clamped pipelines. *Proc. Inst. Mech. Eng.* **1992**, *206*, 129–146. [[CrossRef](#)]
15. Thomas, S.G.; Reid, S.R.; Johnson, W. Large deformations of thin-walled circular tubes under transverse loading-I an experimental survey of the bending of simply supported tubes under a central load. *Int. J. Mech. Sci.* **1976**, *18*, 325–333. [[CrossRef](#)]
16. Plastics Europe. Plastics—The Facts 2019: An Analysis of European Plastics Production, Demand and Waste Data. 2019. Available online: <https://plasticseurope.org/wp-content/uploads/2021/10/2019-Plastics-the-facts.pdf> (accessed on 9 September 2023).
17. Hülsmann, T.; Nowack, R.E. 70 years of experience with PVC pipes. In Proceedings of the PPXII, Milan, Italy, 19–22 April 2004.
18. Teppfa & Pe100+. Position Paper—100 Years Lifetime of Polyethylene Pressure Pipe Systems Buried in the Ground for Water and Natural Gas Supply. 2019. Available online: <https://www.teppfa.eu/wp-content/uploads/TEPPFA-PE100-Position-on-100years-lifetime-of-PE-Pipes-2.pdf> (accessed on 9 September 2023).
19. Alferink, F. The experience with the use of UPVC pipes in various buried applications. In Proceedings of the PPXVIII, Berlin, Germany, 12–14 September 2016.
20. Folkman, S. Validation of the long life of PVC pipes. In Proceedings of the PPXVII, Chicago, IL, USA, 22–24 September 2014.
21. Weller, J.; Hermkens, R.; van der Stok, E. The remaining quality of the PVC gas grid results of 10 years of on-going research. In Proceedings of the PPXVIII, Berlin, Germany, 12–14 September 2016.
22. Cohen, B.R. Fixing America’s Crumbling Underground Water Infrastructure. Competitive Enterprise Institute. 2012. Available online: <https://cei.org/issue-analysis/fixing-americas-crumbling-underground-water-infrastructure> (accessed on 14 January 2019).
23. Folkman, S. Water Main Break Rates in the USA and Canada: A Comprehensive Study. Mechanical and Aerospace Engineering Faculty Publications, Paper 174. 2018. Available online: [https://digitalcommons.usu.edu/mae\\_facpub/174](https://digitalcommons.usu.edu/mae_facpub/174) (accessed on 24 January 2019).
24. Carroll, M.M. Polyvinyl chloride (PVC) pipe reliability and failure modes. *Reliab. Eng.* **1985**, *13*, 11–21. [[CrossRef](#)]
25. Davis, P.; Burn, S.; Moglia, M.; Gould, S. A physical probabilistic model to predict failure rates in buried PVC pipelines. *Reliab. Eng. Syst. Saf.* **2007**, *92*, 1258–1266. [[CrossRef](#)]
26. Balkaya, M.; Moore, I.D.; Sağlam, A. Study of non-uniform bedding support under continuous PVC water distribution pipes. *Tunn. Undergr. Space Technol.* **2013**, *35*, 99–108. [[CrossRef](#)]
27. Frank, A.; Messiha, M.; Koch, T.; Poduška, J.; Hutař, P.; Arbeiter, F.; Pinter, G. Correlation of the cyclic cracked round bar test and hydrostatic pressure test for unplasticized polyvinylchloride. *Polym. Test.* **2021**, *95*, 107125. [[CrossRef](#)]
28. Costa, Y.D.J.; Zornberg, J.G.; Costa, C.M.L. Physical modeling of buried PVC pipes overlying localized ground subsidence. *Acta Geotech.* **2021**, *16*, 807–825. [[CrossRef](#)]
29. Lucchi, M.; Lorenzini, M. Effects of pipe angular velocity and oven configuration on tube temperature distribution in the radiative heating of PVC pipes. *Int. J. Energy Environ. Eng.* **2018**, *9*, 123–134. [[CrossRef](#)]

30. Ariyoshi, M.; Tanaka, Y.; Izumi, A.; Kawabata, T. In Situ and Laboratory Testing of Small Diameter PVC Irrigation Pipes for Investigation of Fatigue Failure. *Transp. Infrastruct. Geotechnol.* **2018**, *5*, 59–74. [[CrossRef](#)]
31. *ASTM D638-14*; Standard Test Method for Tensile Properties of Plastics. ASTM: West Conshohocken, PA, USA, 2022.
32. *GB/T14152-2001*; Thermoplastics Pipes—Determination of Resistance to External Blows—Round the Clock Method. General Administration of Quality Supervision, Inspection and Quarantine of the People Republic of China: Beijing, China, 2001.
33. *ASTM D7136*; Standard Test Method for Measuring the Damage Resistance of a Fiber-Reinforced Polymer Matrix Composite to a Drop-Weight Impact Event. ASTM: West Conshohocken, PA, USA, 2020.
34. Reid, S.R. Metal tubes as impact energy absorbers. In *Metal Forming and Impact Mechanics: William Johnson Commemorative Volume*; Oxford: Pergamon, Turkey, 1985; pp. 249–269.
35. Dassault Systèmes. ABAQUS 6.14 Analysis User's Guide, Volume III: Materials. USA. 2014. Available online: [http://130.149.89.49:2080/v6.14/pdf\\_books/ANALYSIS\\_3.pdf](http://130.149.89.49:2080/v6.14/pdf_books/ANALYSIS_3.pdf) (accessed on 1 September 2023).
36. Richardson, M.O.W.; Wishear, M.J. Review of low-velocity impact properties of composite materials. *Compos. A Appl. Sci. Manuf.* **1996**, *27A*, 1123–1131. [[CrossRef](#)]

**Disclaimer/Publisher's Note:** The statements, opinions and data contained in all publications are solely those of the individual author(s) and contributor(s) and not of MDPI and/or the editor(s). MDPI and/or the editor(s) disclaim responsibility for any injury to people or property resulting from any ideas, methods, instructions or products referred to in the content.